# Ultrathin Wetting Layer-Free Plasmonic Gold Films

Robert Lemasters[1,*], Cheng Zhang[2,3,*,#], Manoj Manjare[1], Wenqi Zhu[2,3], Junyeob Song[2,4], Sergei Urazhdin[1], Henri J. Lezec[2], Amit Agrawal[2,3], and Hayk Harutyunyan[1,#]

1. Department of Physics, Emory University, Atlanta, GA, 30322, USA

2. Physical Measurement Laboratory, National Institute of Standards and Technology, Gaithersburg, MD, 20899, USA

3. Maryland Nanocenter, University of Maryland, College Park, MD, 20742, USA

4. Department of Electrical and Computer Engineering, Virginia Tech, Blacksburg, VA 24061, USA

* Equal contributors

# Corresponding authors:

cheng.zhang@nist.gov

hayk.harutyunyan@emory.edu

**Abstract**

Ultrathin gold films are attractive for plasmonic and metamaterial devices, thanks to their useful optical and optoelectronic properties. However, deposition of ultrathin continuous Au films of few nanometer thickness is challenging and generally requires wetting layers, resulting in increased optical losses and incompatibility with optoelectronic device requirements. We demonstrate wetting layer-free plasmonic gold films with thicknesses down to 3 nm obtained by deposition on substrates cooled to cryogenic temperatures. We systematically study the effect of substrate temperature on the properties of the deposited Au films, and show that substrate cooling suppresses the Vomer-Webber growth mode of Au, promoting early-stage formation of continuous Au films with improved surface morphology and enhanced optoelectronic properties. Our results pave the way for straightforward implementation of ultrathin Au-based optoelectronic and plasmonic devices, as well as metamaterials and metasurfaces.

**Keywords**: *plasmonics, thin films, metamaterials, gold, cryogenic deposition*

## Introduction

Nanoscale thin metal films are essential for the implementation of many nanophotonic and plasmonic devices [1-6]. The most common metals employed for applications in the visible and near-infrared optical range are silver (Ag) and gold (Au), due to their low optical loss. These metals also feature a large negative part of the permittivity in this frequency range, enabling the occurrence of surface plasmon polaritons (SPPs) at their interfaces [7]. Au is significantly more chemically stable than Ag, making it the material of choice for a variety of applications including plasmonic interconnects [8], modulators [9], resonators [10], sensors [11-12], and metamaterials [13-14].

In applications utilizing SPPs, optical loss is approximately inversely proportional to the thickness of the metallic layer, because of the scaling of the fraction of the total modal energy localized in the thin metal film. While performance improvement at small film thicknesses comes at a cost of reduced field confinement, the latter is not essential for many applications. For instance, the loss in a long-range SPP waveguide, embedded in free space, is reduced by a factor of 20 when the metal thickness is reduced from 50 nm to 5 nm, even though the field spillover into free space increases from 300 nm to 1.5 μm for the long-range antisymmetric mode with the free-space wavelength of 780 nm [8] (see Supporting Information, Fig. S1). The reduction in loss with thinner metal films is true if only the ohmic losses in an ideal metal slab are considered. In practice, scattering from impurities, defects, or surface roughness become the dominant damping channel in the ultrathin metal film regime [15].

Thin metallic films are also advantageous for their use as transparent and flexible electrodes in optoelectronic devices such as photovoltaics, diodes and photodetectors [16-20]. Furthermore, they find applications in metal-dielectric heterostructures with hyperbolic or negative index response [21]. In such systems, optical loss diminishes with decreasing thickness of interstitial metal layers. Moreover, using the effective medium approximation is more valid for thin films as they better mimic a homogenous medium [22]. Finally, as the thickness of the metal layer reaches few monolayers, the resulting strong confinement can lead to the emergence of quantum effects, facilitating fundamentally different plasmonic device functionalities [23-24].

Fabrication of continuous ultrathin (< 10 nm) Au films is challenging, because Au grows in the Vomer-Webber (three-dimensional) mode on common substrates such as fused-silica or

silicon [25]. In the initial stage of film growth, the deposited Au atoms cluster together and form isolated islands. As the deposition continues, these isolated islands increase in size, and eventually merge to form a percolated conductive thin Au film. Such a three-dimensional (3D) growth mode leads to a minimum thickness value, commonly referred as the "percolation threshold", below which the deposited Au layer is discontinuous and exhibits a rough surface morphology. The tendency of Au to form clusters has been utilized for the fabrication of low-cost and large-scale plasmonic structures [26-27].

To reduce the percolation threshold of thin Au films and improve their surface morphology, a thin wetting layer of a different material is generally utilized before Au deposition. Among the common wetting layers are metals such as Ti and Cr [28], metal oxides such as copper oxide and Al-doped ZnO [15, 29], organic molecules such as mercapto-silane [30], transition metal dichalcogenides [31], and polymers [32]. While the wetting layers are effective in reducing the percolation threshold and improving the surface morphology of thin Au films, some wetting materials such as Cr and Ti also introduce additional optical losses and potentially make them incompatible with the devices' functional requirements (see Supporting Information, Fig. S2). Furthermore, a recent study shows that an ultrathin Au film with a mass-equivalent thickness as small as 5.4 nm can be prepared using a mercapto-silane wetting layer on fused silica substrate, but due to the interference from this layer, the film's optical transmittance is significantly lower than expected for an ideal Au film of the same mass-equivalent thickness [30]. Finally, wetting layer-free epitaxial growth of crystalline Ag layers has been recently demonstrated on Si substrates with remarkably small thickness and sheet resistivity [33]. However, the need for non-transparent crystalline substrate and complex fabrication method can limit the applications of this method.

The influence of the substrate temperature on the growth of thin metal films is well known [17, 34-37]. Numerous studies have been dedicated to uncover the mechanisms of temperature-dependent growth mechanisms and to find optimal conditions for material deposition. However, most of these studies either have used wetting layers or have metal films deposited on non-transparent substrates such as metals [38-42]. To the best of our knowledge, ultrathin wetting layer-free plasmonic metals on optically transparent substrates, such as fused-silica, have not been reported so far.

Here, we demonstrate that wetting layer-free, ultrathin and plasmonic Au films can be fabricated by deposition directly on fused-silica substrates cooled to cryogenic temperatures. We analyze the effect of substrate temperature on the properties of the deposited ultrathin Au films and find that substrate cooling helps to reduce the mobility of Au atoms on the substrate and thus promotes the formation of ultrathin Au films with improved surface morphology and enhanced optoelectronic characteristics, including lower optical loss and sheet resistance, and higher optical transmittance. We utilize the demonstrated substrate cooling approach to fabricate record-thin, 3 nm thick Au films with good plasmonic properties, i.e., large negative real part and small imaginary part of the permittivity. The ultrathin thickness is further verified by the parameter uniqueness test using spectroscopic ellipsometry. Our work establishes a new practical approach for the fabrication of high-quality wetting layer-free ultrathin Au films, paving the way for their applications in optoelectronic and plasmonic devices, as well as metamaterials and metasurfaces.

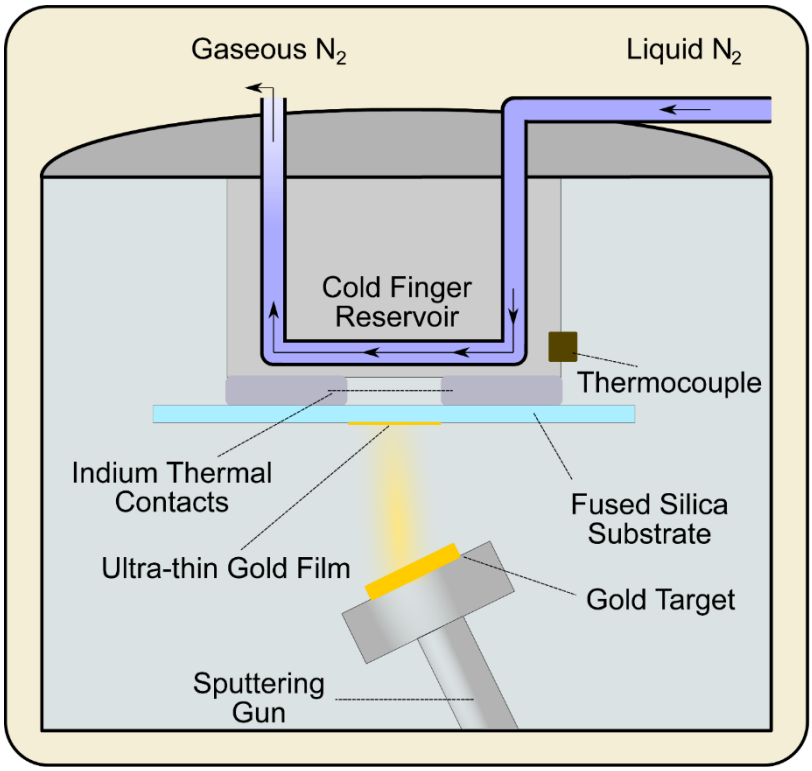


**Figure 1**: Schematic representation of the deposition chamber and the process for the fabrication of ultrathin Au films.

## Results and Discussion

### Deposition of ultrathin Au films at different temperatures

Ultrathin Au films are deposited on 500 μm thick fused-silica substrates, with substrate temperatures ranging from room temperature (23 °C) down to liquid nitrogen (LN) temperature (-195 °C), using magnetron sputtering in high-vacuum chamber with a base pressure of less than $2.7\times10^{-5}$ Pa. The temperature of the substrate are controlled by attaching the sample holder to a cold finger (Fig. 1). To facilitate a good thermal contact between the substrate and cold finger, a 1-mm-thick indium layer is inserted between the sample holder and the edge areas of the substrate. This ensures that no indium residue is left on the central part of the substrate, which would have compromised the subsequent optical characterization of the film. To cool the substrate, LN is siphoned into the cold finger reservoir at a rate of ≈ 400 standard cubic centimeters per minute (sccm). For the lowest temperature used in these experiments, the flow is turned off once the minimum temperature of -195 °C is achieved (as monitored by a thermocouple gauge attached to the sample holder). To consistently achieve intermediate temperatures during deposition, a more involved method was developed. As the LN flow begins to flow and the temperature begins to drop, the LN flow is turned off well before the target temperature is reached. The substrate temperature continued to drop due to the residual LN in the reservoir. Once the temperature stabilizes, this process is repeated with smaller spurts of LN that are allowed to evaporate until the substrate temperature is stabilized just below the target temperature. The natural warming at the calibrated rate of ≈ 1 °C/min then results in the increase of the substrate temperature towards the desired value. This process of lowering the temperature just below the target value and allowing it to warm back up to this value is repeated several times to ensure equilibrium between the cold finger and the substrate at the target temperature value.

After the substrate reaches the target temperature, the Au deposition is performed in 0.4 Pa of ultrapure Argon (Ar), at a rate of 0.5 nm/s determined by a calibrated quartz crystal monitor. The deposited thickness is controlled by the opening time of the mechanical shutter. After the deposition, the sample is kept inside the chamber at the base pressure, until it warmed up to room temperature, to avoid any water vapor condensation or ice crystal formation on the deposited film when exposed to atmosphere. Due to the relatively small difference in the coefficient of thermal expansion of Au and silica substrate and their weak dependence on temperature we do not expect

large compressive strain in our samples. Such strain would lead to the "warping" of the film over microscopic regions, which have not been observed even in the samples fabricated at the lowest temperature of -195 °C.

**Optoelectronic characteristics and surface morphologies of 5 nm thick Au**

The effect of substrate cooling on the optoelectronic properties and surface morphology of the Au films was studied for 5 nm thick films, deposited on fused-silica substrates at temperatures ranging from the room temperature (23 °C) down to the liquid nitrogen temperature (-195 °C). Seven different temperature values are chosen: 23 °C, 0 °C, -30 °C, -50 °C, -80 °C, -120 °C, and -195 °C. The corresponding Au films are denoted as $Au_{23°C}^{5nm}$, $Au_{0°C}^{5nm}$, $Au_{-30°C}^{5nm}$, $Au_{-50°C}^{5nm}$, $Au_{-80°C}^{5nm}$, $Au_{-120°C}^{5nm}$ and $Au_{-195°C}^{5nm}$, respectively.

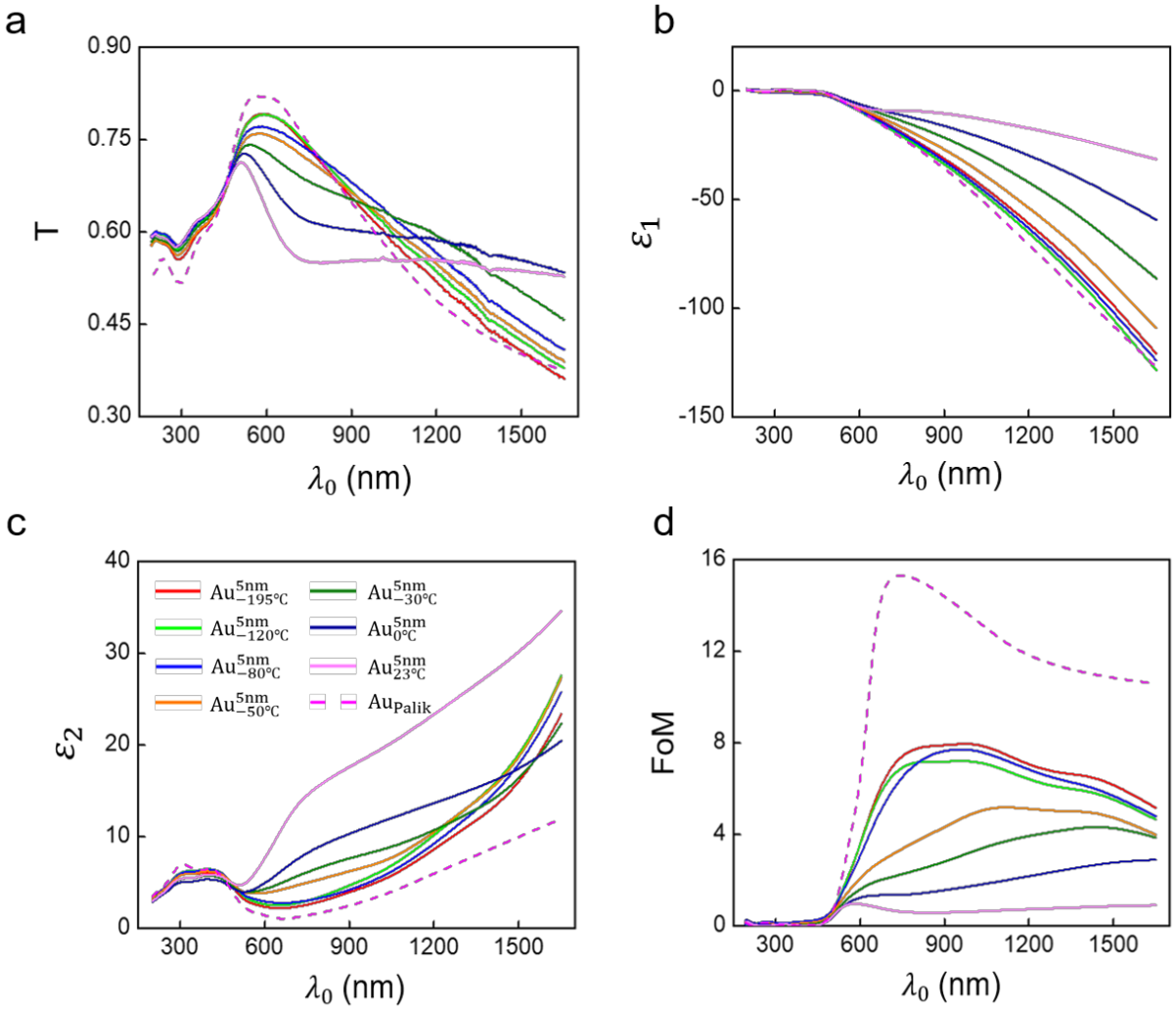


**Figure 2**: (a) Measured transmittance T versus free-space wavelength $\lambda_0$ for samples $Au^{5nm}_{-195°C}$, $Au^{5nm}_{-120°C}$, $Au^{5nm}_{-80°C}$, $Au^{5nm}_{-50°C}$, $Au^{5nm}_{-30°C}$, $Au^{5nm}_{0°C}$, and $Au^{5nm}_{23°C}$. The reference (T = 1) for all measurements is transmittance through air. The calculated transmittance T($\lambda_0$) obtained by transfer matrix method for a 5.66 nm thick Au film on a 500 μm thick fused silica substrate is plotted as well (dashed line). The chosen thickness of 5.66 nm is the same as the measured thickness of sample $Au^{5nm}_{-195°C}$ using spectroscopic ellipsometry. The index of Au employed in the calculation is based on Ref. [43]. (b-c) Measured real (b) and imaginary (c) parts of the relative electric permittivity, $\varepsilon_1$ and $\varepsilon_2$, of samples deposited at -195°C to 23°C. The permittivity of Au film from [43] is plotted for reference (dashed line). (d) FoM = $|\varepsilon_1(\lambda_0)|/\varepsilon_2(\lambda_0)$ for samples deposited at -195°C to 23°C. The FoM calculated based on the permittivity of Au from [43] is plotted for reference (dashed line). Legend of Fig. 2c also applies to Figs. 2a, 2b and 2d.

Spectroscopic ellipsometry is utilized to determine the relative electric permittivity of ultrathin Au samples as a function of free-space wavelength, $\varepsilon_r(\lambda_0) = \varepsilon_1(\lambda_0) + i\varepsilon_2(\lambda_0)$, over the wavelength range from 200 nm to 1650 nm. To precisely characterize the thin semi-transparent absorbing films, the "spectroscopic ellipsometry + transmission (SE + T)" scheme was employed [44-45], where (*i*) the complex electric field reflection coefficients for *s* and *p* polarizations at three different angles of incidence (55°, 65°, and 75°), and (*ii*) optical transmittance at normal incidence, are utilized to extract the complex permittivity and the thickness of the Au layer. In addition, surface morphology of the Au samples was characterized by scanning electron microscopy, and the sheet resistance $R_s$ was measured by the four-point probe method.

The best-fit thickness values along with mean-squared-error (MSE) for different samples determined by spectroscopic ellipsometry are given in Table 1. These values closely match the targeted deposition thickness of 5 nm. The small deviations from this value are likely caused by the fluctuations of the sputtering rate during the deposition of the samples. Similar thickness values are obtained using AFM measurements (see Supporting Information, Fig. S3). The measured transmittance spectra (Fig. 2a) for the two highest temperature samples $Au_{0℃}^{5nm}$ and $Au_{23℃}^{5nm}$ exhibit a broad dip in the wavelength range of ≈ 600 nm to ≈ 1000 nm. This resonant dip can be attributed to the localized surface plasmon absorption of the Au island-like grains in non-percolated films (Figs. 3a and 3b). The detrimental effect of such grains on the film's optical properties is also evidenced in the measured permittivity curves of the two films, shown in Figs. 2b and 2c. Here, the real part of the permittivity exhibits less negative values compared to the films deposited at lower temperatures, indicating a degraded metallic property. Similarly, the imaginary part shows the highest values among all the samples over the large portion of the studied spectral range, suggesting an increased optical absorption.

**Table 1**. Film thicknesses determined by ellipsometry and sheet resistance of the samples.

| | $Au_{-195℃}^{5nm}$ | $Au_{-120℃}^{5nm}$ | $Au_{-80℃}^{5nm}$ | $Au_{-50℃}^{5nm}$ | $Au_{-30℃}^{5nm}$ | $Au_{0℃}^{5nm}$ | $Au_{23℃}^{5nm}$ |
|---|---|---|---|---|---|---|---|
| best-fit thickness, nm | ≈ 5.66 | ≈ 5.06 | ≈ 5.09 | ≈ 5.47 | ≈ 5.85 | ≈ 6.32 | ≈ 5.64 |
| regression-analysis-fitting MSE | 2.742 | 2.789 | 5.698 | 4.706 | 3.653 | 6.866 | 2.765 |

| | | | | | | | |
|---|---|---|---|---|---|---|---|
| averaged sheet resistance, Ω /□, | 15.76 | 19.77 | 22.80 | 23.77 | 31.37 | 42.33 | 70.37 |

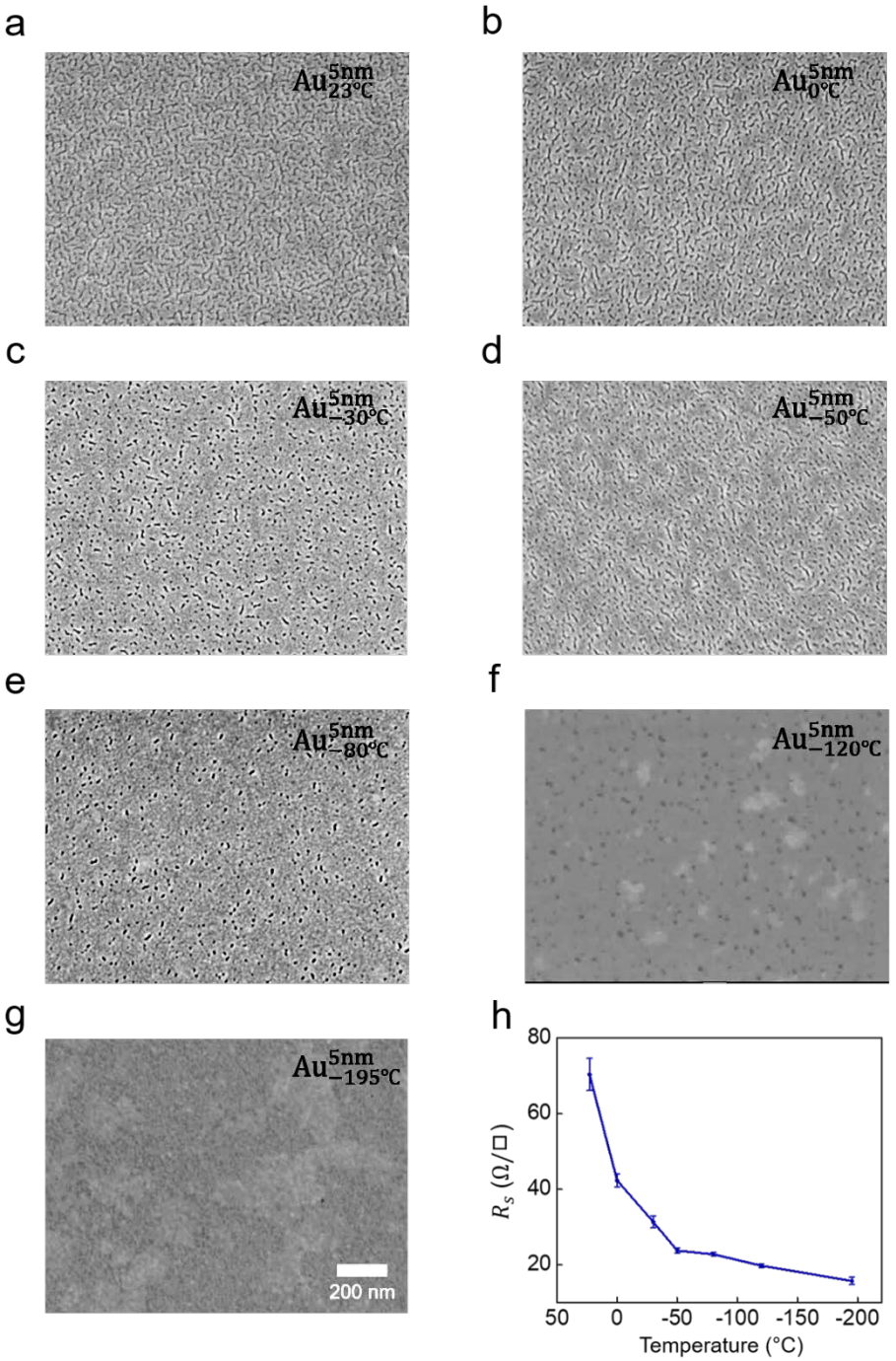

**Figure 3**: (a-g) Scanning electron micrographs (SEMs) of details of sample $Au_{23°C}^{5nm}$ (a), $Au_{0°C}^{5nm}$ (b), $Au_{-30°C}^{5nm}$ (c), $Au_{-50°C}^{5nm}$ (d), $Au_{-80°C}^{5nm}$ (e), $Au_{-120°C}^{5nm}$ (f), and $Au_{-195°C}^{5nm}$ (g). Scale bar of Fig. 3g applies to Figs. 3a to 3f. (h) Measured sheet resistance of the ultrathin Au film as a function of deposition temperature. Error bars show one standard deviation of the measured data obtained from several consecutive measurements.

For the samples deposited at the reduced substrate temperature, the absorption dip corresponding to the localized surface plasmon resonance gradually diminishes, and transmittance of the film improves, in particular for the wavelength range from 500 nm to 800 nm (Fig. 2a). It is worth noting that in these samples, the relatively lower transmittance at longer wavelengths is not due to the increased optical absorption of the film, but rather due to the increased reflection, hinting at improved metallic property of the deposited Au film. Monitoring the surface morphology using SEM imaging also further confirms this picture. Reducing the substrate temperature from $Au_{-30°C}^{5nm}$ to $Au_{-120°C}^{5nm}$, results in gradually reduced void spots on the film, finally leading to a void-free film for $Au_{-195°C}^{5nm}$ sample (Figs. 3c to 3g). In contrast to the high substrate temperature samples, the measured transmittance curve for $Au_{-195°C}^{5nm}$ does not exhibit localized surface plasmon resonance. Its peak amplitude and spectral shape are in a good agreement with the theoretical transmittance spectrum of a continuous, 5.66 nm thick Au film on fused-silica substrate, calculated using transfer matrix method (Fig. 2a). The thickness of 5.66 nm used in the theoretical transmittance calculations matches the thickness of sample $Au_{-195°C}^{5nm}$ experimentally determined from the spectroscopic ellipsometry. Here, the complex permittivity values for Au used in the calculations (plotted as dashed lines in Figs. 2b and 2c), were taken from a common reference for the permittivity of the bulk Au material [43]. Gradually decreasing the substrate temperature leads to a more negative real part of the permittivity $\varepsilon_1$ (improved metallic properties of the film) and a gradual decrease of the imaginary part $\varepsilon_2$, *i.e.* reduced losses. The figure of merit FoM = $|\varepsilon_1(\lambda_0)|/\varepsilon_2(\lambda_0)$, which characterizes the quality of the plasmonic film [46], increases with decreasing deposition temperature over the same wavelength range (Fig. 2d). Finally, the improved optoelectronic properties of ultrathin Au films are further evidenced by the measured sheet resistance of the film (Fig. 3h), which monotonically decreases as the deposition temperature decreases. The averaged sheet resistance values of the samples are given in Table 1. Aging of the samples are observed over 6 months period where the sheet resistance deteriorates by ~30% for

samples kept in a nitrogen-purged sample box. The annealing at 120°C and 150°C temperatures does not have any significant effects on the sheet resistance of the samples (see Supporting Information, Fig. S4). Interestingly, the absence of wetting layer in our samples does not significantly affect their adhesion to the substrate (see Supporting Information, Fig. S5). The optical (permittivity) and electrical (sheet resistance) methods are chosen to characterize our samples since these measurements provide the most technologically relevant information about the averaged optoelectronic properties of our samples. However, to quantitatively study the morphology of the samples atomic force microscopy (AFM) imaging are performed. The roughness analysis and topographic patterns provided by these measurements are in a good agreement with other characterization methods used in this study (see Supporting Information, Fig. S6). Namely, root mean square (RMS) roughness of the films monotonically increases with the deposition temperature, with $\mathrm{Au}^{5\mathrm{nm}}_{-195\mathrm{C}^{\circ}}$ exhibiting the smoothest surface.

Based on the results presented above, we conclude that at the early stages of metal deposition, isolated nanoscopic metal clusters begin to nucleate and eventually begin to coalesce and increase in size [17]. This is followed by the percolation, and eventually the formation of a continuous film. The coalescence process of the initial clusters is driven by the minimization of the surface free energy of the system [47]. In this process, smaller clusters with larger relative surface areas diffuse on the surface, and coalesce in a "liquid-like" manner into bigger clusters with smaller relative surface areas, lowering the total surface free energy [48]. This makes three-dimensional metal growth thermodynamically more likely than two-dimensional surface growth on the metal-oxide interface given that the metal-metal cohesion is much stronger than metal-oxide adhesion. Surface quality features are therefore determined by how large the coalescing clusters can get before wetting the surface at the percolation threshold followed by continuous film formation [34]. If the percolation threshold can be reached sooner, then smaller film features should follow. Cooling down the substrate decreases the diffusion rate of the metal atoms, thus, enabling the formation of stable metal nanoclusters of smaller sizes. This suppresses the 3D clustering and favors the formation of percolated ultrathin metal films. Similarly, faster deposition rates facilitate the formation of continuous films which is evidenced by slight improvement of the optical losses (see Supporting Information, Fig. S7). To determine the crystalline sizes in our ultrathin films we have also performed X-ray diffraction (XRD) measurements. The crystalline

sizes are estimated from the widths of the X-ray peaks using Scherrer equation (see Supporting Information, Fig. S8). Based on this analysis, it appears that lower temperature of the substrate results in smaller crystallites, in consistence with our diffusion suppression growth picture. However, we must note that the crystalline sizes determined by this method are very close to the 5 nm thickness of the film. Thus, it is plausible that the widths of the peaks are mainly determined by the film thickness.

**Plasmonic 3-nm-thick Au films**

Leveraging the beneficial effect of substrate cooling on the formation of ultrathin Au films, as revealed by the study described above, we further explore the possibility of realizing even thinner plasmonic Au films. A nominally 3 nm thick film, $Au^{3nm}_{-195°C}$, is deposited on fused silica substrate at the liquid nitrogen temperature (deposition rate: 0.5 nm/s), and characterized by spectroscopic ellipsometry, scanning electron microscopy and four-point probe method.

Compared to the nominally 5 nm thick Au film prepared at the same temperature ($Au^{5nm}_{-195°C}$), sample $Au^{3nm}_{-195°C}$ exhibits a higher transmittance over the spectral range of the measurement (200 nm to 1650 nm), thanks to its reduced film thickness (Fig. 4a). Meanwhile, it also exhibits degraded relative electric permittivity compared to $Au^{5nm}_{-195°C}$. This is manifested by a smaller negative real part of measured permittivity, $\varepsilon_1$, and a larger positive imaginary part of measured permittivity, $\varepsilon_2$ (Fig. 4b). Nevertheless, the measured $\varepsilon_1$ still monotonically decreases beyond 450 nm, confirming the plasmonic behavior of the film. The degraded optical properties could be attributed to the defects remaining from the early stage of the continuous film formation, as evidenced by the void spots in the SEM images (Fig. 4c). The averaged sheet resistance is 124.42 Ω/□. The best-fit thickness value determined from spectroscopic ellipsometry is ≈ 2.95 nm, closely matching the targeted thickness value of 3 nm. The measurements done on samples with 4 nm thickness show that gradual deterioration of the film properties is observed at 3-5 nm thickness range (see Supporting Information, Fig. S9).

Finally, we perform parameter uniqueness test to further verify the achieved record-small thickness of 2.95 nm for a wetting layer-free gold film. During the test, we first choose the

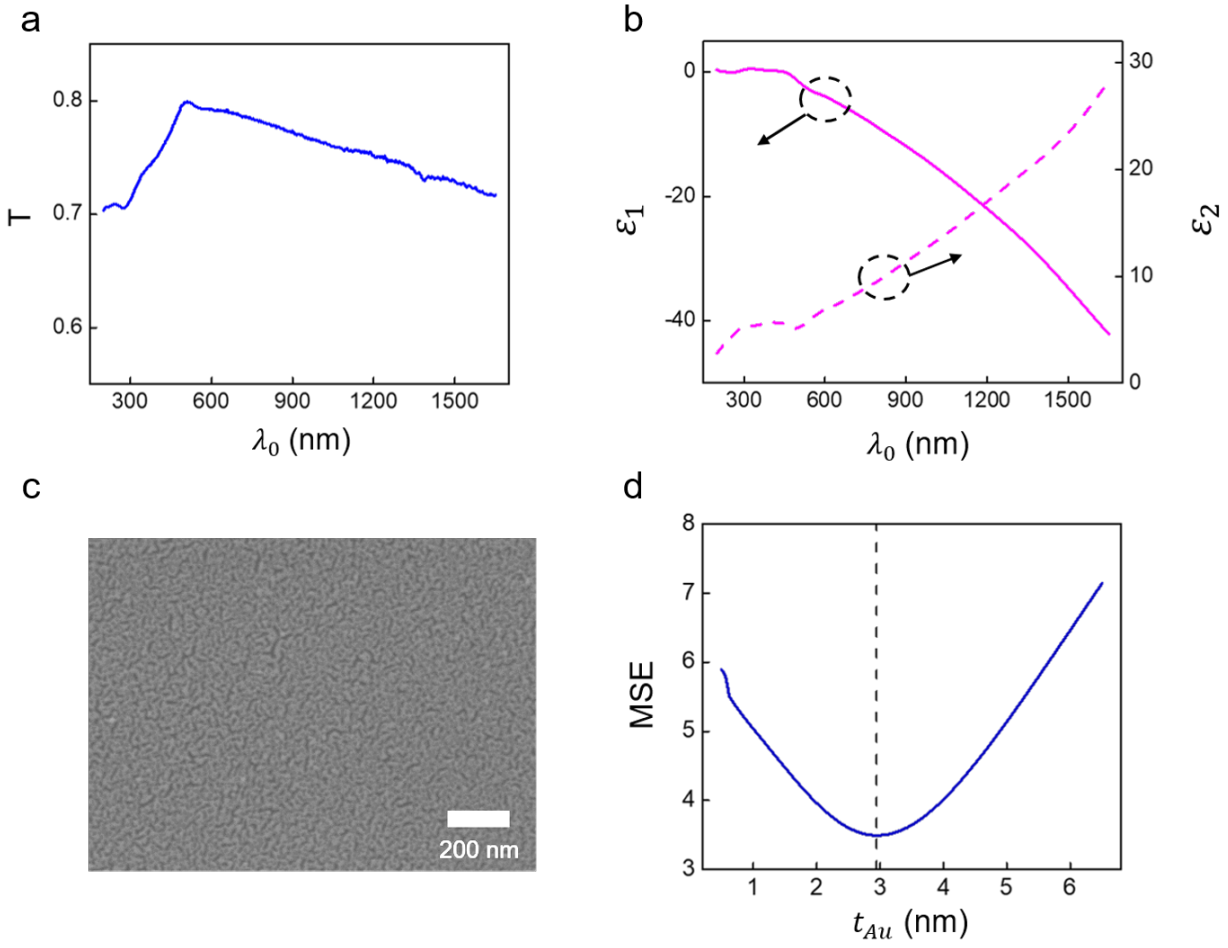


**Figure 4**: (a) Measured transmittance T versus free-space wavelength $\lambda_0$ for sample $Au^{5nm}_{-195℃}$ deposited on a 500 μm thick fused silica substrate. The reference (T = 1) for this measurements is transmittance through air. (b) Measured real (solid line) and imaginary (dashed line) parts of the relative electric permittivity, $\varepsilon_1$ and $\varepsilon_2$, of samples $Au^{3nm}_{-195℃}$. (c) SEM of details of sample $Au^{3nm}_{-195℃}$. (d) Parameter uniqueness test of the thickness of the Au film of sample $Au^{3nm}_{-195℃}$. The dashed line denotes the best-fit thickness value $t_{Au}$ = 2.95 nm.

thickness of the Au film ($t_{Au}$) as a test parameter, define a set of 100 test values (evenly spaced between 0.5 nm and 6.5 nm) around its best-fit value ($t_{Au}$ = 2.95 nm), and then compute the corresponding regression-analysis-fitting MSE in ellipsometry. In the computation, $t_{Au}$ is fixed at each test value, whereas all the other model parameters are allowed to vary, and the resulting MSE($t_{Au}$) is recorded. Such a uniqueness test generates a plot of the MSE versus the pre-defined

test parameter values of $t_{Au}$. As shown in Fig. 4d, the curve of MSE($t_{Au}$) displays a well-defined minimum around the best-fit value of 2.95 nm. This suggests that the measured film thickness is reliable and uniquely defined, since no other combination of the remaining fit parameters is able to produce a similar MSE for the ellipsometry characterization.

**Conclusion:**

We systematically studied the effect of substrate temperature on the optoelectronic properties and surface morphology of thin Au films deposited on fused silica. We showed that cooling down the substrate suppresses the Vomer-Webber growth mode of Au, enabling the formation of ultrathin continuous Au films with enhanced optoelectronic properties and improved surface morphologies. Wetting layer-free, plasmonic Au films down to the measured layer thickness of 2.95 nm were achieved by depositing the films on a substrate at the liquid nitrogen temperature. Our work suggests a new approach to the fabrication of wetting layer-free and high-quality ultrathin Au films, which could benefit various Au-based optoelectronic and plasmonic devices, as well as metamaterials and metasurfaces.

**Methods:**

**Preparation of deposition substrate:** Fused-silica substrates were cleaned by sonication in deionized water and detergent, acetone, and isopropyl alcohol sequentially for 20 minutes at room temperature. The substrates were then dried with nitrogen and then transferred into the sputtering chamber.

**Spectroscopic ellipsometry characterization:** The ellipsometry characterization of deposited Au films is performed using M-2000 ellipsometer (J. A. Woollam Co. Inc.), and data analysis is performed using the CompleteEASE software (J. A. Woollam Co. Inc.). The frequency-dependent permittivity value of each sample is modeled by a combination of Gaussian, Tauc-Lorentz and Drude oscillators.

**SEM, AFM, XRD and 4-probe characterization**: SEM characterization tool used in this study was JEOL 7800F Field Emission Scanning Electron Microscope. AFM imaging was performed

on Bruker Dimension FastScan Atomic Force Microscope. The 4 point resistance measurements were done on Four Dimensions 280DI sheet resistance mapping system. Grazing incidence XRD measurement were performed on Rigaku SmartLab X-ray diffraction system (Copper K-α line at 1.5406 Å). The angle of incidence was 0.7°, scan speed was set as 1°/min, and the scan step was 0.05°.

**Sample Disclaimer:** Certain commercial equipment, instruments, or materials are identified in this paper in order to specify the experimental procedure adequately. Such identification is not intended to imply recommendation or endorsement by the National Institute of Standards and Technology, nor is it intended to imply that the materials or equipment identified are necessarily the best available for the purpose.

**Acknowledgements:** R. Lemasters and H. Harutyunyan acknowledge support from DoE (DE-SC0020101). C. Zhang, W. Zhu, and A. Agrawal acknowledge support under the Cooperative Research Agreement between the University of Maryland and the National Institute of Standards and Technology Center, Award #70NANB14H209, through the University of Maryland. S. Urazhdin acknowledges support from NSF (ECCS-1804198 and DMR-1504449). C. Zhang acknowledges helpful discussions with Dr. N. Hong.

**Supporting Information**. Simulated mode profiles of long range surface plasmon polaritons, optical properties of samples with an adhesion layer, film thickness determined by AFM measurements, resistivity measurements assessing the aging and annealing effects, tests assessing the adhesion of the films, AFM measurements of surface roughness for samples deposited at various temperatures, optical properties of samples deposited at different rates, XRD measurement on films deposited at different temperatures, properties of 4 nm films.

**References**


1. Meinzer, N.; Barnes, W. L.; Hooper, I. R., Plasmonic meta-atoms and metasurfaces. *Nat. Photonics* **2014,** *8*, 889.

2. Poddubny, A.; Iorsh, I.; Belov, P.; Kivshar, Y., Hyperbolic metamaterials. *Nat. Photonics* **2013,** *7*, 948.

3. Genevet, P.; Capasso, F.; Aieta, F.; Khorasaninejad, M.; Devlin, R., Recent advances in planar optics: from plasmonic to dielectric metasurfaces. *Optica* **2017,** *4*, 139-152.

4. McPeak, K. M.; Jayanti, S. V.; Kress, S. J. P.; Meyer, S.; Iotti, S.; Rossinelli, A.; Norris, D. J., Plasmonic Films Can Easily Be Better: Rules and Recipes. *ACS Photonics* **2015,** *2*, 326-333.

5. Nagpal, P.; Lindquist, N. C.; Oh, S.-H.; Norris, D. J., Ultrasmooth Patterned Metals for Plasmonics and Metamaterials. *Science* **2009,** *325*, 594-597.

6. Zhang, C.; Zhao, D.; Gu, D.; Kim, H.; Ling, T.; Wu, Y.-K. R.; Guo, L. J., An Ultrathin, Smooth, and Low-Loss Al-Doped Ag Film and Its Application as a Transparent Electrode in Organic Photovoltaics. *Adv. Mater.* **2014,** *26*, 5696-5701.

7. Maier, S. A., Plasmonics: Fundamentals and Applications. **2007**.

8. Berini, P., Long-range surface plasmon polaritons. *Adv. Opt. Photonics* **2009,** *1*, 484-588.

9. Haffner, C.; Chelladurai, D.; Fedoryshyn, Y.; Josten, A.; Baeuerle, B.; Heni, W.; Watanabe, T.; Cui, T.; Cheng, B.; Saha, S.; Elder, D. L.; Dalton, L. R.; Boltasseva, A.; Shalaev, V. M.; Kinsey, N.; Leuthold, J., Low-loss plasmon-assisted electro-optic modulator. *Nature* **2018,** *556*, 483-486.

10. Zhu, W.; Xu, T.; Wang, H.; Zhang, C.; Deotare, P. B.; Agrawal, A.; Lezec, H. J., Surface plasmon polariton laser based on a metallic trench Fabry-Perot resonator. *Sci. Adv.* **2017,** *3*, e1700909.

11. Stockman, M. I., Nanoplasmonic sensing and detection. *Science* **2015,** *348*, 287-288.

12. Mayer, K. M.; Hafner, J. H., Localized Surface Plasmon Resonance Sensors. *Chem. Rev.* **2011,** *111*, 3828-3857.

13. Yu, N.; Genevet, P.; Kats, M. A.; Aieta, F.; Tetienne, J.-P.; Capasso, F.; Gaburro, Z., Light Propagation with Phase Discontinuities: Generalized Laws of Reflection and Refraction. *Science* **2011,** *334*, 333-337.

14. Zhang, C.; Pfeiffer, C.; Jang, T.; Ray, V.; Junda, M.; Uprety, P.; Podraza, N.; Grbic, A.; Guo, L. J., Breaking Malus' law: Highly efficient, broadband, and angular robust asymmetric light transmitting metasurface. *Laser Photonics Rev.* **2016,** *10*, 791-798.

15. Maniyara, R. A.; Rodrigo, D.; Yu, R.; Canet-Ferrer, J.; Ghosh, D. S.; Yongsunthon, R.; Baker, D. E.; Rezikyan, A.; García de Abajo, F. J.; Pruneri, V., Tunable plasmons in ultrathin metal films. *Nat. Photonics* **2019,** *13*, 328-333.

16. O'Connor, B.; Haughn, C.; An, K.-H.; Pipe, K. P.; Shtein, M., Transparent and conductive electrodes based on unpatterned, thin metal films. *Appl. Phys. Lett.* **2008,** *93*, 223304.

17. Yun, J., Ultrathin Metal films for Transparent Electrodes of Flexible Optoelectronic Devices. *Adv. Funct. Mater.* **2017,** *27*, 1606641.

18. Pode, R. B.; Lee, C. J.; Moon, D. G.; Han, J. I., Transparent conducting metal electrode for top emission organic light-emitting devices: Ca–Ag double layer. *Appl. Phys. Lett.* **2004,** *84*, 4614-4616.

19. Hecht, D. S.; Hu, L.; Irvin, G., Emerging Transparent Electrodes Based on Thin Films of Carbon Nanotubes, Graphene, and Metallic Nanostructures. *Adv. Mater.* **2011,** *23*, 1482-1513.

20. Zhang, C.; Huang, Q.; Cui, Q.; Ji, C.; Zhang, Z.; Chen, X.; George, T.; Zhao, S.; Guo, L. J., High-Performance Large-Scale Flexible Optoelectronics Using Ultrathin Silver Films with Tunable Properties. *ACS Appl. Mater. Interfaces* **2019,** *11*, 27216-27225.

21. Smolyaninov, I. I., Hyperbolic Metamaterials. Morgan & Claypool Publishers: 2018. http://dx.doi.org/10.1088/978-1-6817-4565-7.

22. Subramania, G.; Fischer, A. J.; Luk, T. S., Optical properties of metal-dielectric based epsilon near zero metamaterials. *Appl. Phys. Lett.* **2012,** *101*, 241107.

23. Vidal, G.; Latorre, J. I.; Rico, E.; Kitaev, A., Entanglement in Quantum Critical Phenomena. *Phys. Rev. Lett.* **2003,** *90*, 227902.

24. Qian, H.; Xiao, Y.; Liu, Z., Giant Kerr response of ultrathin gold films from quantum size effect. *Nat. Commun.* **2016,** *7*, 13153.

25. Sennett, R. S.; Scott, G. D., The Structure of Evaporated Metal Films and Their Optical Properties. *JOSA* **1950,** *40*, 203-211.

26. Doron-Mor, I.; Barkay, Z.; Filip-Granit, N.; Vaskevich, A.; Rubinstein, I., Ultrathin Gold Island Films on Silanized Glass. Morphology and Optical Properties. *Chem. Mater.* **2004,** *16*, 3476-3483.

27. Tesler, A. B.; Chuntonov, L.; Karakouz, T.; Bendikov, T. A.; Haran, G.; Vaskevich, A.; Rubinstein, I., Tunable Localized Plasmon Transducers Prepared by Thermal Dewetting of Percolated Evaporated Gold Films. *J. Phys. Chem. C* **2011,** *115*, 24642-24652.

28. Todeschini, M.; Bastos da Silva Fanta, A.; Jensen, F.; Wagner, J. B.; Han, A., Influence of Ti and Cr Adhesion Layers on Ultrathin Au Films. *ACS Appl. Mater. Interfaces* **2017,** *9*, 37374-37385.

29. Xie, J.; Bi, Y.; Ye, M.; Rao, Z.; Shu, L.; Lin, P.; Zeng, X.; Ke, S., Epitaxial ultrathin Au films on transparent mica with oxide wetting layer applied to organic light-emitting devices. *Appl. Phys. Lett.* **2019,** *114*, 081902.

30. Kossoy, A.; Merk, V.; Simakov, D.; Leosson, K.; Kéna-Cohen, S.; Maier, S. A., Optical and Structural Properties of Ultra-thin Gold Films. *Adv. Opt. Mater.* **2015,** *3*, 71-77.

31. Yakubovsky, D. I.; Stebunov, Y. V.; Kirtaev, R. V.; Ermolaev, G. A.; Mironov, M. S.; Novikov, S. M.; Arsenin, A. V.; Volkov, V. S., Ultrathin and Ultrasmooth Gold Films on Monolayer MoS2. *Adv. Mater. Interf.* **2019,** *0*, 1900196.

32. Leosson, K.; Ingason Arni, S.; Agnarsson, B.; Kossoy, A.; Olafsson, S.; Gather Malte, C., Ultra-thin gold films on transparent polymers. In *Nanophotonics*, 2013; Vol. 2, p 3.

33. Abd El-Fattah, Z. M.; Mkhitaryan, V.; Brede, J.; Fernández, L.; Li, C.; Guo, Q.; Ghosh, A.; Echarri, A. R.; Naveh, D.; Xia, F.; Ortega, J. E.; García de Abajo, F. J., Plasmonics in Atomically Thin Crystalline Silver Films. *ACS Nano* **2019,** *13*, 7771-7779.

34. Campbell, C. T., Ultrathin metal films and particles on oxide surfaces: structural, electronic and chemisorptive properties. *Surf. Sci. Rep* **1997,** *27*, 1-111.

35. Kaiser, N., Review of the fundamentals of thin-film growth. *Appl. Opt.* **2002,** *41*, 3053-3060.

36. Diebold, U.; Pan, J. M.; Madey, T. E., Growth mode of ultrathin copper overlayers on ${\mathrm{TiO}}_{2}$(110). *Phys. Rev. B* **1993,** *47*, 3868-3876.

37. Zhang, T. C.; Mei, Z. X.; Guo, Y.; Xue, Q. K.; Du, X. L., Influence of growth temperature on formation of continuous Ag thin film on ZnO surface by ultra-high vacuum deposition. *J. Phys. D: Appl. Phys.* **2009,** *42*, 065303.

38. Egelhoff, W. F.; Jacob, I., Reflection High-Energy Electron Diffraction (RHEED) Oscillations at 77 K. *Phys. Rev. Lett.* **1989,** *62*, 921-924.

39. Sergeant, N. P.; Hadipour, A.; Niesen, B.; Cheyns, D.; Heremans, P.; Peumans, P.; Rand, B. P., Design of Transparent Anodes for Resonant Cavity Enhanced Light Harvesting in Organic Solar Cells. *Adv. Mater.* **2012,** *24*, 728-732.

40. Stefaniuk, T.; Wróbel, P.; Górecka, E.; Szoplik, T., Optimum deposition conditions of ultrasmooth silver nanolayers. *Nanoscale Res. Lett.* **2014,** *9*, 153.

41. van der Vegt, H. A.; van Pinxteren, H. M.; Lohmeier, M.; Vlieg, E.; Thornton, J. M. C., Surfactant-induced layer-by-layer growth of Ag on Ag(111). *Phys. Rev. Lett.* **1992,** *68*, 3335-3338.

42. Jing, D.; Ünal, B.; Qin, F.; Yuen, C.; Evans, J. W.; Jenks, C. J.; Sordelet, D. J.; Thiel, P. A., Stranski–Krastanov-like growth of an Ag film on a metallic glass. *Thin Solid Films* **2009,** *517*, 6486-6492.

43. Lynch, D. W.; Hunter, W. R., Comments on the Optical Constants of Metals and an Introduction to the Data for Several Metals. In *Handbook of Optical Constants of Solids*, Palik, E. D., Ed. Academic Press: Burlington, 1997; pp 275-367.

44. Zhang, C.; Hong, N.; Ji, C.; Zhu, W.; Chen, X.; Agrawal, A.; Zhang, Z.; Tiwald, T. E.; Schoeche, S.; Hilfiker, J. N.; Guo, L. J.; Lezec, H. J., Robust Extraction of Hyperbolic Metamaterial Permittivity Using Total Internal Reflection Ellipsometry. *ACS Photonics* **2018,** *5*, 2234-2242.

45. Secondo, R.; Fomra, D.; Izyumskaya, N.; Avrutin, V.; Hilfiker, J. N.; Martin, A.; Özgür, Ü.; Kinsey, N., Reliable modeling of ultrathin alternative plasmonic materials using spectroscopic ellipsometry [Invited]. *Opt. Mater. Express* **2019,** *9*, 760-770.

46. Kinsey, N.; Ferrera, M.; Naik, G. V.; Babicheva, V. E.; Shalaev, V. M.; Boltasseva, A., Experimental demonstration of titanium nitride plasmonic interconnects. *Opt. Express* **2014,** *22*, 12238-12247.

47. Parker, S. C.; Campbell, C. T., Kinetic model for sintering of supported metal particles with improved size-dependent energetics and applications to Au on ${\mathrm{TiO}}_{2}(110)$. *Phys. Rev. B* **2007,** *75*, 035430.

48. José-Yacamán, M.; Gutierrez-Wing, C.; Miki, M.; Yang, D. Q.; Piyakis, K. N.; Sacher, E., Surface Diffusion and Coalescence of Mobile Metal Nanoparticles. *J. Phys. Chem. B* **2005,** *109*, 9703-9711.

**For Table of Contents Use Only**

Ultrathin Wetting Layer-Free Plasmonic Gold Films

Robert Lemasters, Cheng Zhang, Manoj Manjare, Wenqi Zhu, Junyeob Song, Sergei Urazhdin, Henri J. Lezec, Amit Agrawal, and Hayk Harutyunyan

Table of Contents (TOC) entry:

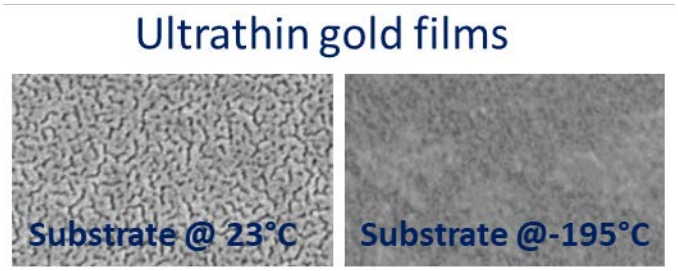


The TOC entry shows the morphology of ultrathin gold films deposited at two different temperatures of the fused silica substrate. Cryogenic deposition of the material results in smoother and more continuous films. Ultrathin metal films can find applications as transparent and flexible electrodes in sustainable energy harvesting devices.

# Supporting Information

## Ultrathin Wetting Layer-Free Plasmonic Gold Films

Robert Lemasters[1,*], Cheng Zhang[2,3,*,#], Manoj Manjare[1], Wenqi Zhu[2,3], Junyeob Song[2,4], Sergei Urazhdin[1], Henri J. Lezec[2], Amit Agrawal[2,3], and Hayk Harutyunyan[1,#]

1. Department of Physics, Emory University, Atlanta, GA, 30322, USA

2. Physical Measurement Laboratory, National Institute of Standards and Technology, Gaithersburg, MD, 20899, USA

3. Maryland Nanocenter, University of Maryland, College Park, MD, 20742, USA

4. Department of Electrical and Computer Engineering, Virginia Tech, Blacksburg, VA 24061, USA

**6 pages, 9 figures.**

**Supporting Information Section S1:**

Mode analysis of long-range surface plasmon polaritons (LRSPPs) on 5-nm-thick and 50-nm-thick Au films are performed at the wavelength of 780 nm using Lumerical finite-difference time-domain simulation package. The lowest-order LRSPP mode on a 50-nm-thick, 10-μm-wide Au stripe embedded in glass (assuming refractive index of 1.45) shows an effective refractive of 1.451, a propagation loss of ≈ 63 dB/cm, and a 1/e out-of-plane decay length of ≈ 500 μm. The lowest-order LRSPP mode on a 5-nm-thick, 10-μm-wide Au stripe embedded in glass shows an effective refractive of 1.450, a propagation loss of ≈ 3.4 dB/cm, and a 1/e out-of-plane decay length of ≈ 2.7 μm. The LRSPPs mode intensity profiles in both cases are shown in Fig. S1.

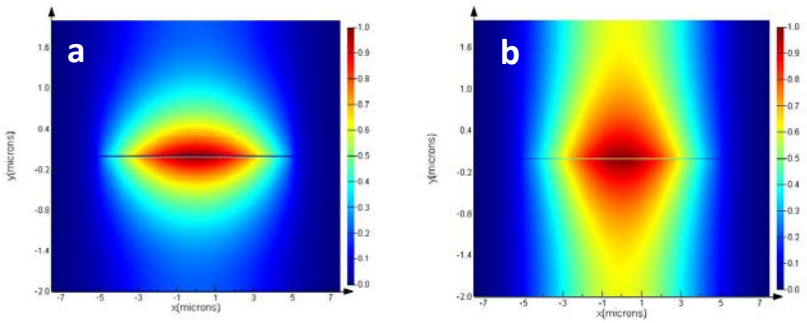


**Fig. S1**. Simulated mode intensity profiles of LRSPPs on (a) 50-nm-thick and (b) 5-nm-thick, 10-μm-wide Au stripes at the wavelength of 780 nm

**Supporting Information Section S2:**

Typically, adhesion layers degrade the optical properties of the samples. To demonstrate this we have fabricated a 5 nm Au sample with a 1 nm Cr wetting layer and have compared the it's permittivity with that of the $Au^{5nm}_{-195℃}$ sample. As it can be seen from the figure below, the real part of the permittivity becomes less negative whereas the imaginary part increases.

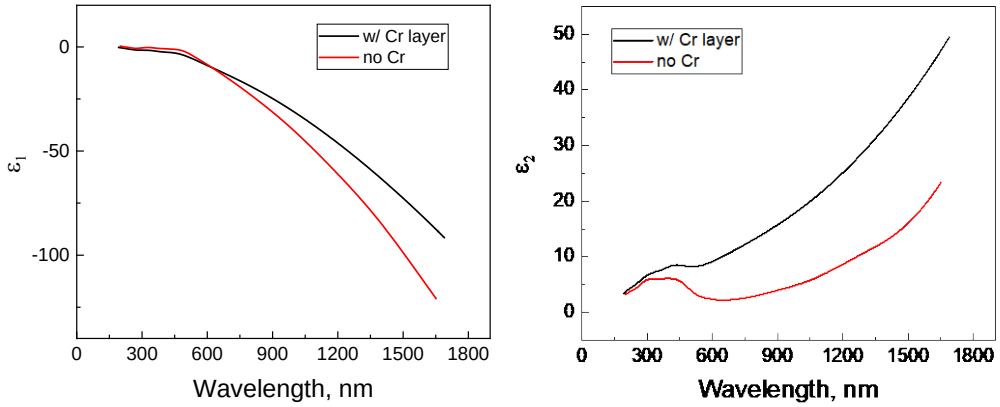


**Fig. S2.** The real (left panel) and imaginary (right panel) parts of the permittivity for two samples: 5nm Au deposited at -195°C (red line) and 1nm Cr / 5nm Au deposited at -195°C (black line). Cr layer introduces additional loss as evidenced by larger imaginary part of permittivity.

**Supporting Information Section S3:**

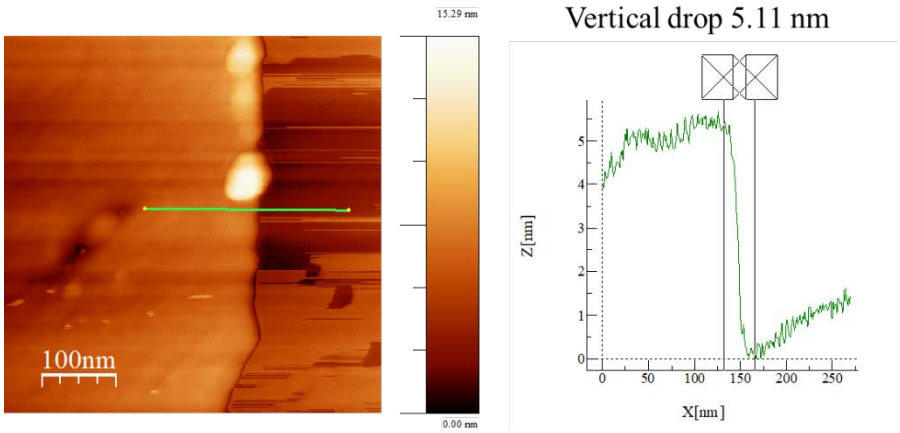


**Fig. S3**. Film thickness determined by AFM measurements. AFM scan (left panel) and cross section (right panel). The thickness value of 5.11 nm agrees well with the ellipsometry measurements.

**Supporting Information Section S4:**

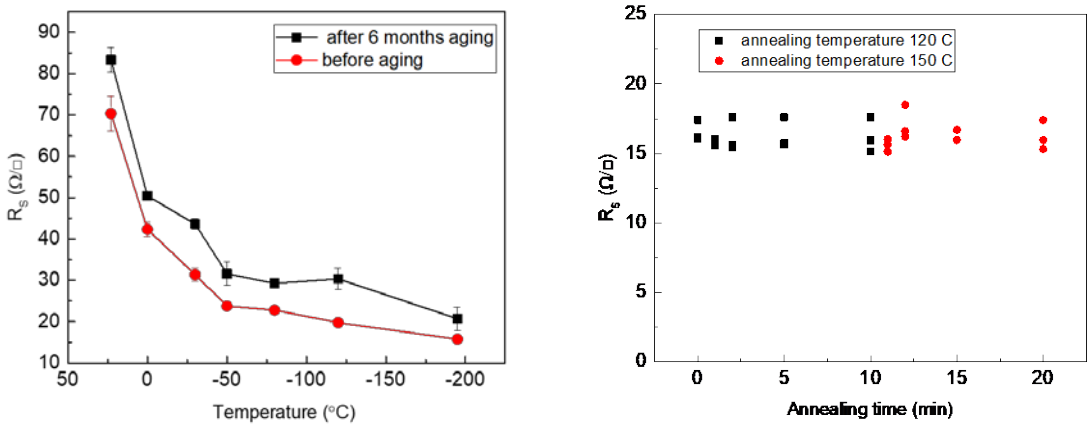


**Fig. S4.** The effects of aging (left panel) and annealing (right panel) of the samples. The sheet resistance deteriorates by ~30% over 6 months storage in a nitrogen-purged sample box. The annealing at 120 C and 150 C temperatures does not have any significant effects on the sheet resistance of the samples.

**Supporting Information Section S5:**

To test the adhesion of the Au films we apply Kapton tape to each sample, press to have a good contact between the tape and the Au film, and then peel off the tape. The results of these simple assessments after 3 peeling attempts are shown in the photographs shown in Fig. S5. No noticeable changes are visible on the films that are fabricated with and without 1 nm Cr adhesion layer.

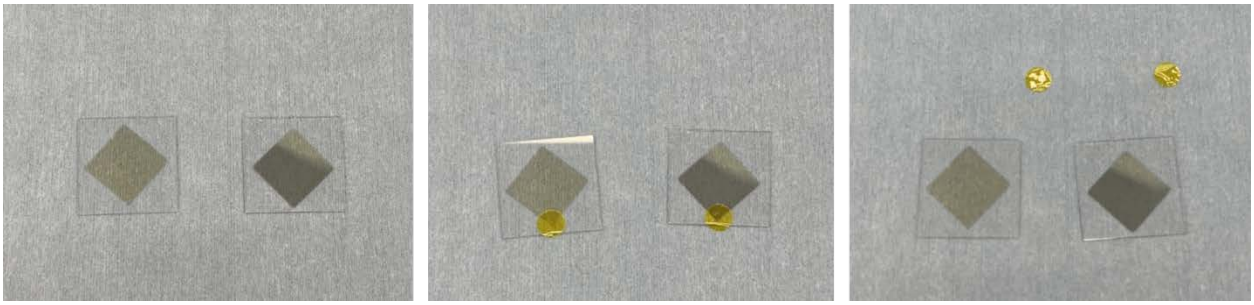

**Fig. S5**. Photographs of two 5 nm Au samples with and without 1nm Cr adhesion layer. The left panel shows the films before the application of the adhesive tape, the middle panel shows the application of the tape, and the right panel shows the films after the adhesive tape have been peeled off. The procedure has been applied for 3 times.

**Supporting Information Section S6:**

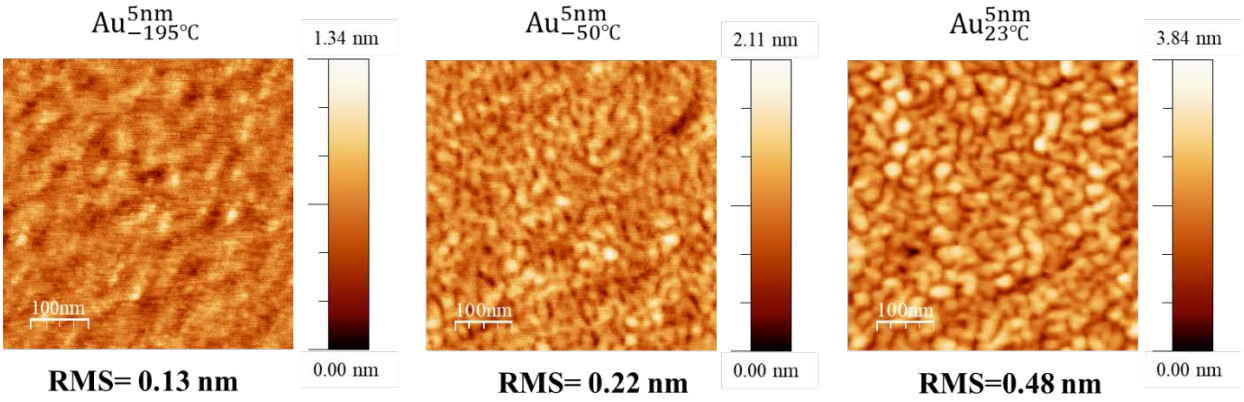


**Fig. S6**. AFM images of three samples deposited at different temperatures. The RMS roughness of the topography monotonically increases with the deposition temperature confirming that the cryogenic deposition of the 5 nm Au yields continuous films.

**Supporting Information Section S7:**

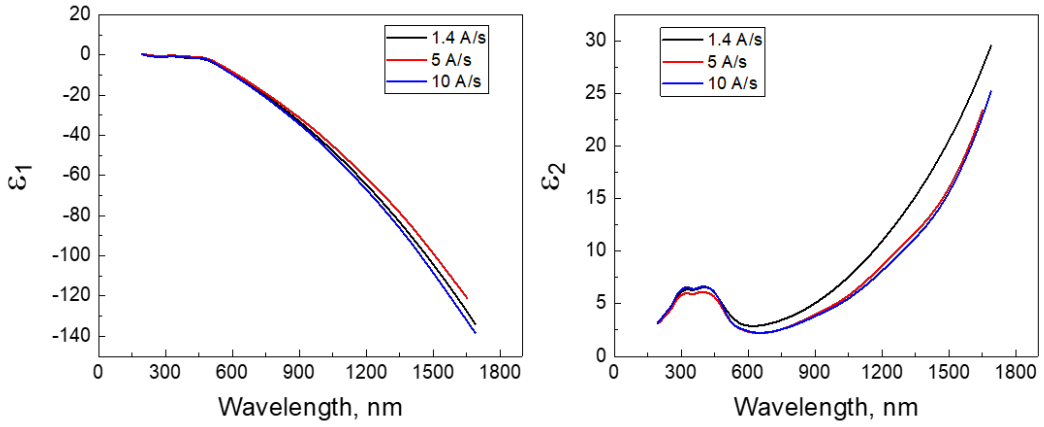


**Fig. S7.** The optical properties of $Au^{5nm}_{-195℃}$ samples deposited at three different rates: 1.4 Å/s (black line), 5 Å/s (red line), 10 Å/s (blue line). Lower rates of 1.4 Å/s result in slightly larger optical loss.

**Supporting Information Section S8:**

Here we estimate the crystalline size of the films using X-ray diffraction (XRD). Fig. S8 shows the results of our XRD measurements on three 5nm samples fabricated at -195C, -50C and 23C. Given the ultrathin nature of the films the spectra have considerable background however several peaks corresponding to

various crystalline directions are visible. The position of the peaks perfectly correspond to gold diffraction peaks (such as (111), (200), (220) and so on). Based on the width of these 2θ resonances one can estimate the crystallite size in the films using Scherrer equation $L = \frac{k\lambda}{B(2\theta)\cos\theta}$, where $L$ is the crystallite size, $k$=0.89 is a constant, $\lambda$= 1.54 Å is the wavelength of the X-rays, $B$ is the width of the peak, and $\theta$ is the incidence angle.

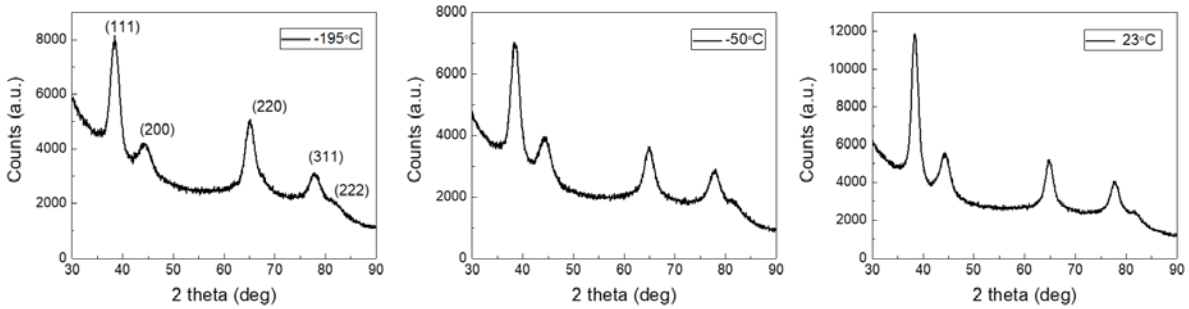


**Fig. S8**. XRD measurements on $Au^{5nm}_{-195°C}$ (left panel), $Au^{5nm}_{-50°C}$(middle panel) and $Au^{5nm}_{23°C}$ (right panel) samples.

Using the widths of (111) and (220) peaks we have estimated the crystalline size $L$ for all three samples. The results of are shown in the table below:

| | θ (deg) | B(2θ) (deg) | L (nm) |
|---|---|---|---|
| $Au^{5nm}_{23°C}$ (111) | 38.28 | 1.59 | 5.25 |
| $Au^{5nm}_{23°C}$ (220) | 64.73 | 1.89 | 4.92 |
| $Au^{5nm}_{-50°C}$ (111) | 38.35 | 2.1 | 3.96 |
| $Au^{5nm}_{-50°C}$ (220) | 64.79 | 2.39 | 3.96 |
| $Au^{5nm}_{-195°C}$ (111) | 38.34 | 2.18 | 3.82 |
| $Au^{5nm}_{-195°C}$ (220) | 65.14 | 2.49 | 3.74 |

**Supporting Information Section S9:**

The samples with 4 nm thickness show that gradual deterioration of the film properties is observed at 3-5 nm thickness range. The sheet resistivity is 49 Ω/□, which is in-between the values observed for $Au^{5nm}_{-195°C}$ (15.76 Ω/□) and $Au^{3nm}_{-195°C}$ (124.42 Ω/□).

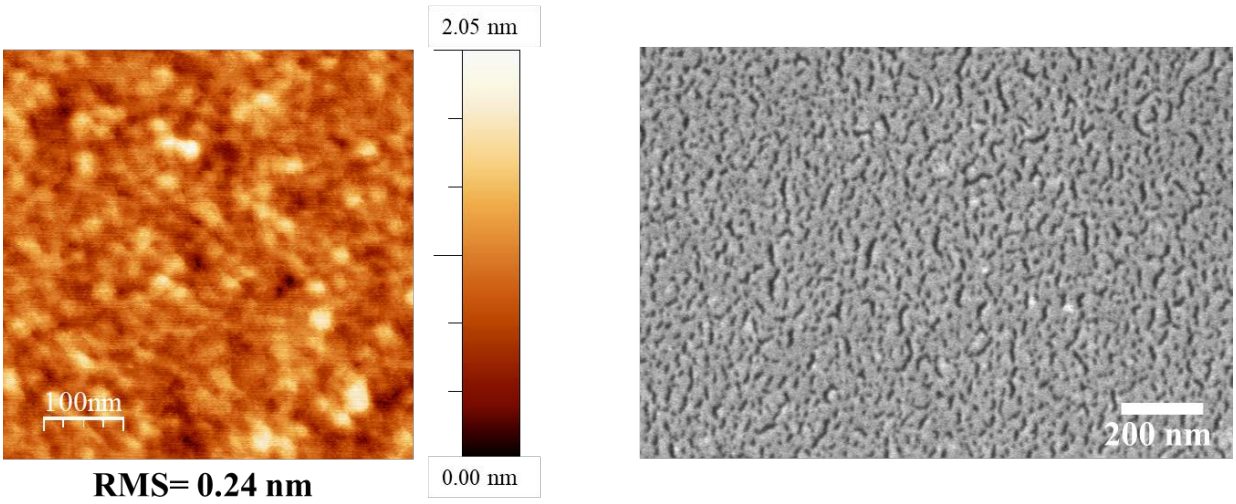


**Fig. S9**. AFM (left panel) and SEM images of 4 nm Au film ($Au^{4nm}_{-195°C}$). The topography shows deteriorated RMS roughness compared to the 5 nm films. The sheet resistance of this sample is 49 Ω/□.